A Parameterized Linear 3D Magnetic Equivalent Circuit for Analysis and Design of Radial Flux Magnetic Gears–Part I: Implementation

Matthew Johnson, *Member, IEEE*, Matthew C. Gardner, *Member, IEEE*, Hamid A. Toliyat, *Fellow, IEEE*

***Abstract*--Magnetic gears can perform the same function as mechanical gears with the added benefits inherent to contactless power transfer. However, quick and accurate analysis tools are required for magnetic gears to reach their full potential. As end effects can significantly impact the slip torque of a magnetic gear, 2D models often overestimate the slip torques, so 3D models are frequently required. Therefore, this paper proposes a 3D linear Magnetic Equivalent Circuit (MEC) or reluctance network model of radial flux magnetic gears with surface mounted magnets. This is an extension of a previously developed 2D MEC model, and, like the previous 2D model, it is thoroughly parametrized so that it can be directly applied to a wide range of parametric cases. This is Part I of a two-part paper and focuses on the implementation of the 3D MEC model. Part II compares the 3D MEC model against nonlinear finite element analysis (FEA) models to validate the MEC model's accuracy and to develop guidelines for discretizing the geometry.**

***Index Terms*--end effects, finite element analysis, magnetic equivalent circuit, magnetic gear, optimization, permeance network, radial flux, reluctance network, torque density.**

I. Introduction

MAGNETIC gears transfer mechanical power between high-torque, low-speed rotation and low-torque, high-speed rotation. However, whereas magnetic gears perform the same function as mechanical gears, magnetic gears utilize the interaction of magnetic fields instead of interlocking teeth to transfer power between rotors. This noncontact operation gives magnetic gears a plethora of potential advantages, including inherent overload protection, reduced maintenance requirements, higher reliability, decreased acoustic noise, and physical isolation between the shafts. These potential advantages have spurred significant recent research [1]-[4] in magnetic gears for various applications, including electric aircraft propulsion [5], wind [6] and wave [7] energy generation, ship propulsion [8], and electric vehicles [9].

Nevertheless, magnetic gears still struggle to compete with their mechanical counterparts with respect to basic metrics such as size, weight, and cost [10]. To make magnetic gears more competitive and allow them to realize their potential advantages, it is necessary to be able to conduct detailed, application-specific parametric optimizations [11]-[13]. The tools used to analyze magnetic gears include finite element analysis (FEA) models, analytical models, winding function theory (WFT), and magnetic equivalent circuit (MEC) or reluctance network models. FEA models are most commonly used because of their accuracy, robustness, and flexibility, but they can be computationally intensive and slow. WFT and analytical models are significantly faster than FEA but less accurate and flexible. MEC models offer a compromise between the speed of WFT and analytical models and the robustness and accuracy of FEA models. To investigate the advantages of MEC models, the authors previously implemented [14] and evaluated [15] a parameterized linear 2D MEC model for radial flux magnetic gears with surface permanent magnets, as shown in Fig. 1. The evaluation of the linear 2D MEC model demonstrated that it was significantly faster than a commercial finite element analysis (FEA) package and very accurate for most practical designs [15].

Another significant advantage of MECs is that they are

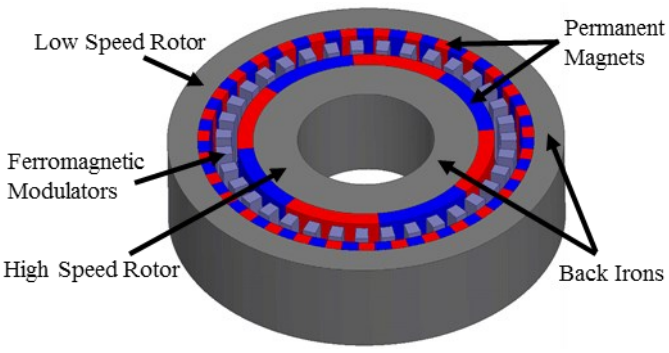

Fig. 1. Radial flux magnetic gear with surface permanent magnets.

This work was supported in part by the U.S. Army Research Laboratory and was accomplished under Cooperative Research and Development Agreement# 14-10. The views and conclusions contained in this document are those of the authors and should not be interpreted as representing the official policies, either expressed or implied, of the Army Research Laboratory or the U.S. Government. The U.S. Government is authorized to reproduce and distribute reprints for Government purposes notwithstanding any copyright notation herein.

M. Johnson is with the U.S. Army Research Laboratory, College Station, TX 77843 USA (e-mail: matthew.c.johnson186.civ@mail.mil).

M. C. Gardner is with the Electric Powertrains Lab at the University of Texas at Dallas, Richardson, TX 75080 USA (e-mail: Matthew.Gardner@utdallas.edu).

H. A. Toliyat is with the Advanced Electric Machines and Power Electronics Lab at Texas A&M University, College Station, TX 77843 USA (e-mail: toliyat@tamu.edu).

well suited for development of 3D models, and a few studies have even suggested that MEC models' advantages of reduced computational intensity and faster simulation times become even more pronounced compared to FEA models when these analysis techniques are extended to 3D models [16]-[18]. This is especially important for analysis of magnetic gears, as 3D effects are generally more significant in magnetic gears than in traditional electric machines due to the strong MMFs of the magnets, which oppose each other in some places, the large equivalent air gaps, and the axial leakage flux paths provided by the modulators [19]. Thus, 2D magnetic gear models frequently predict significantly higher torque ratings than those predicted by 3D models and measured on physical prototypes [11], [19]-[21]. Furthermore, one study even demonstrated that 2D and 3D magnetic gear models can yield different optimum cross-sectional gear designs [12].

This is Part I of a two-part study which extends the generalized 2D parametric linear MEC model of the coaxial radial flux magnetic gear topology implemented in [14] and evaluated in [15] to a full 3D model. The coaxial radial flux magnetic gear shown in Fig. 1 consists of three rotors: the inner high speed rotor (HSR) with P_{HS} permanent magnet pole pairs, the outer low speed rotor (LSR) with P_{LS} permanent magnet pole pairs, and the intermediate modulator rotor with Q_M ferromagnetic pole pieces. The number of modulators should be the sum of the number of pole pairs on the high speed rotor and low speed rotor, as given by

$$Q_M = P_{HS} + P_{LS}. \tag{1}$$

If the modulators are fixed, the HSR and LSR speeds are related by the gear ratio according to

$$\text{Gear Ratio}\big|_{\omega_{Mods}=0} = \frac{\omega_{HS}}{\omega_{LS}} = \frac{-P_{LS}}{P_{HS}} \tag{2}$$

where ω_{HS}, ω_{LS}, and ω_{Mods} are the speeds of the HSR, LSR, and modulators, respectively. Alternatively, if the LSR is fixed and the modulators rotate instead, then the gear ratio becomes positive and increases in magnitude by one to

$$\text{Gear Ratio}\big|_{\omega_{LSR}=0} = \frac{\omega_{HS}}{\omega_{Mods}} = \frac{Q_M}{P_{HS}}. \tag{3}$$

As detailed in [14], the concept of MECs, which are also known as reluctance networks, dates back into the 1800s [22]. In particular, Hopkinson's Law,

$$\mathcal{F} = \mathcal{R}\Phi \tag{4}$$

was formulated by 1886 and relates the scalar magnetic potential or MMF, $\mathcal{F}$, drop across a flux tube to the reluctance, $\mathcal{R}$, of the flux tube and the magnetic flux, Φ, flowing through it. This is analogous to Ohm's Law in electrical circuits. Many past studies [23]-[37] and books [38]-[40] demonstrated the enticing balance of speed and accuracy that MEC models can offer for analysis of electric machines. Furthermore, MECs have been used to analyze rotary magnetic gears and magnetically geared machines [41]-[46] and linear magnetic gears [47]. However, none of these previous magnetic gear MECs systematically evaluated detailed 3D flux paths.

This paper builds on these works and the authors' previous 2D MEC model [14] to present a more flexible and robust 3D approach than the conventional MECs used for electric machine analysis. Rather than using a relatively small number of flux tubes, as in Ostovic's pioneering MEC models of electric machines, which represented each tooth with a single flux tube [25]-[27], [37], [38], the proposed MEC systematically creates a parametric 3D mesh of the geometry, including space axially beyond the gear. This facilitates scaling the number of flux tubes based on the gear geometry and allows accurate modeling of the complex flux paths, rich harmonic content, and end-effects, which are more significant in a magnetic gear than most conventional electric machines, across a wide range of parametric designs. This generally results in many more flux tubes than conventional MECs. This approach most resembles the 3D MEC models of Amrhein and Krein [16]-[18], [32] and Hlioui et al. [37], but those works provide limited information about the matrix representation of the 3D aspects of the implementation. This paper provides a thorough description of a unique parametric 3D flux tube distribution implementation that enables higher accuracy over a wider range of designs. Part I of this two-part paper describes how this 3D MEC can be implemented by combining scaled permeances from 2D cross-sections to reduce the number of necessary permeance calculations.

II. The 3D Node Cell

The systematic, parameterized 2D MEC implementation presented in [14] and [15] can easily be extended to a 3D model in order to characterize the impacts of end effects. The 3D MEC mesh is systematically formed by using the same angular and radial layers employed in the 2D MEC and further subdividing the system geometry into axial or z-coordinate layers (ZL). Each intersection of a radial layer, an angular layer, and an axial layer defines a 3D node cell similar to those described in [16]-[18], [32], and [37]. Every 3D node cell consists of two radially directed permeances, two tangentially directed permeances, and two axially directed permeances, each of which is connected to the center node of the cell and one of the cell's radial, tangential, or axial boundaries, as shown in Fig. 2. The radial and tangential permeances, as well as the radially injected fluxes from the permanent magnets, are calculated in the same manner as for the 2D MEC [14]. A conceptual illustration of an axially oriented

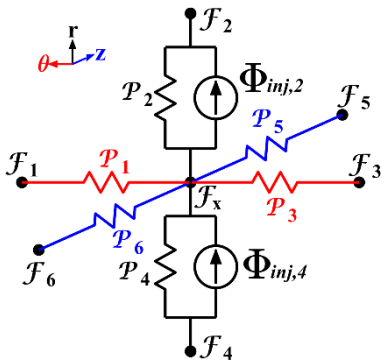

Fig. 2. Annotated 3D node cell schematic.

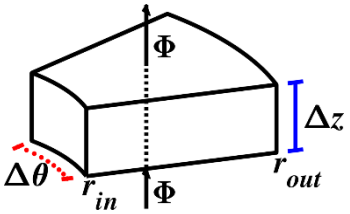

Fig. 3. Conceptual illustration of an axially oriented flux tube.

flux tube is provided in Fig. 3 and the formula for the permeance of each axially directed flux tube, $\mathcal{P}_{ax}$, is given by

$$\mathcal{P}_{ax} = \int_{r_{in}}^{r_{out}} \frac{\mu \cdot \Delta\theta \cdot r \cdot dr}{\Delta z} = \left(\frac{\mu \cdot \Delta\theta}{2 \cdot \Delta z}\right)(r_{out}^2 - r_{in}^2). \quad (5)$$

Each axially directed flux tube corresponds to the full radial width of its node cell, the full angular width of its node cell, and half of the axial height of its node cell. Thus, r_{in} indicates the inner radius of the flux tube, r_{out} denotes the outer radius of the flux tube, $\Delta\theta$ is the uniform angular width of the flux tube (in radians), Δz is the uniform axial height of the flux tube, and μ is the permeability of the flux tube material.

Applying Gauss's law for magnetism to each 3D node cell in the full MEC, such as the one depicted in Fig. 2, yields a node MMF equation of the form given by

$$\sum_{i=1}^{6} \mathcal{P}_i \mathcal{F}_x - \sum_{i=1}^{6} \mathcal{P}_i \mathcal{F}_i = -\Phi_{inj,2} + \Phi_{inj,4}. \quad (6)$$

This expression can be rearranged into the form of

$$\Phi_{x,2D} + \sum_{i=5}^{6} \mathcal{P}_i \mathcal{F}_x - \sum_{i=5}^{6} \mathcal{P}_i \mathcal{F}_i = -\Phi_{inj,2} + \Phi_{inj,4}, \quad (7)$$

which clearly demonstrates the relationship between the basic 3D MEC node MMF equation and the basic 2D node MMF equation given by (12) in [14]. The first term in (7), $\Phi_{x,2D}$, is defined by

$$\Phi_{x,2D} = \sum_{i=1}^{4} \mathcal{P}_i \mathcal{F}_x - \sum_{i=1}^{4} \mathcal{P}_i \mathcal{F}_i \quad (8)$$

as the algebraic sum of all fluxes flowing out of node x due to the MMFs of nodes in the same axial layer and it is equal to the entire left side of the 2D MEC node MMF equation given by (12) in [14]. The second term on the left side of (7) is simply the product of the sum of all axially directed permeances attached to the target node (node "x") and the MMF of the target node, $\mathcal{F}_x$. The third term in (7) represents the algebraic sum of the axial flux components flowing out of node x due to the axially directed permeances attached to node x and the MMFs of the corresponding axially adjacent nodes. As in the 2D MEC node MMF equation, the terms on the right side correspond to the algebraic sum of the injected flux sources flowing into the target node.

The use of 3D node cells is effectively equivalent to building the full 3D MEC by stacking 2D MEC layers on top of each other and connecting corresponding nodes in adjacent 2D MEC layers (adjacent axial layers) with axially directed permeances. The 3D MEC schematic snippet in Fig. 4 illustrates this layering arrangement for the eight node cells formed by the intersection of two adjacent angular layers, two adjacent axial layers, and two adjacent radial layers. The 3D MEC model includes both the gear geometry and a defined region of nonmagnetic material axially beyond the gear. The total number of axial layers, N_{ZL}, in the 3D MEC is the sum of the number of axial layers in the gear, N_{LIG}, and the number of axial layers outside of (axially beyond) the gear, N_{LOG}, which are both independent user-controlled parameters, in addition to the 8 other 2D MEC mesh discretization parameters introduced in [14]. Also, because tighter axial resolution is generally required at the axial ends of the gear, relative to the axial middle of the gear, the distribution of the axial heights of the various axial layers is not necessarily uniform and can be directly specified as needed for different designs. Finally, in addition to the periodic symmetry exhibited by certain designs, the basic radial flux magnetic gear topology always has symmetry about the z plane corresponding to the axial middle of the gear such that no axial flux crosses the axial middle of the gear. Since this is true for all ideal designs (assuming negligible axial misalignment), only one axial half of the gear stack is considered in this implementation of the 3D MEC model to reduce the necessary number of axial layers. The full 3D MEC solution information is then obtained by repeating the "half-stack" model results. This solution is exactly equivalent to that which would be obtained by including the full axial stack in the 3D model.

Each node in the 3D MEC corresponds to a node MMF equation of the same basic form as the one shown in (6) or (7) and there are N_{3D} total nodes in a 3D MEC model, where N_{3D} is the product of the number of angular layers, the total number of radial layers, and the total number of axial layers. Thus, the resulting system of linear equations for the full 3D MEC model can be expressed by the matrix equation

$$\mathcal{P}_{3D}\mathcal{F}_{3D} = \Phi_{3D}, \quad (9)$$

where $\mathcal{P}_{3D}$ is the (N_{3D} x N_{3D}) 3D system permeance matrix, $\mathcal{F}_{3D}$ is the (N_{3D} x 1) column vector of unknown MMFs for each corresponding node in the 3D MEC, and Φ_{3D} is the (N_{3D} x 1) column vector of the algebraic sums of the injected fluxes entering each corresponding node in the 3D MEC. The i^{th} row in $\mathcal{P}_{3D}$ corresponds to the i^{th} node in the MEC and contains the permeance coefficients for that node's MMF equation, such as those shown on the left side of (6). The j^{th} column in $\mathcal{P}_{3D}$ also

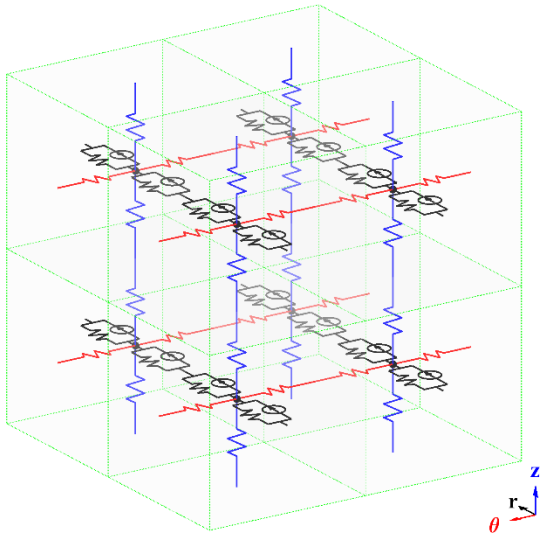

Fig. 4. Construction of 3D MEC from axially connected 2D MEC layers.

corresponds to the j^{th} node in the MEC. Entry $\mathcal{P}_{3D(i,j)}$ in $\mathcal{P}_{3D}$ contains the permeance coefficient which describes the impact of the j^{th} node's MMF on the net flux leaving the i^{th} node. Each diagonal entry, $\mathcal{P}_{3D(i,i)}$, in $\mathcal{P}_{3D}$ contains the positive sum of all equivalent permeances attached directly to the i^{th} node. The permeance coefficient of $\mathcal{F}_x$ in (6) is an example of a diagonal entry in the matrix representation of the system of equations. Each diagonal entry indicates the impact of the corresponding node's MMF on the net flux leaving that node. Each off-diagonal entry $\mathcal{P}_{3D(i,j)}$ in $\mathcal{P}_{3D}$ (entries where $i \neq j$) contains the negative value of the equivalent permeance directly connecting the i^{th} and j^{th} nodes. If there is no direct connection between the i^{th} and j^{th} nodes (a permeance path that does not go through another node), then the corresponding entry in $\mathcal{P}_{3D}$ is zero. The permeance coefficients of $\mathcal{F}_1$, $\mathcal{F}_2$, $\mathcal{F}_3$, $\mathcal{F}_4$, $\mathcal{F}_5$, and $\mathcal{F}_6$ in (6) are examples of off-diagonal entries in the matrix representation of the system of equations.

Alternatively stated, since each row in $\mathcal{P}_{3D}$ corresponds to an equation in the form of (6), the i^{th} row in $\mathcal{P}_{3D}$ has six negative entries corresponding to the permeances directly connecting the i^{th} node to the 6 adjacent nodes. However, nodes on the axial and radial boundaries of the model do not have 6 adjacent nodes, so the rows corresponding to these nodes have fewer negative entries. In every row, the diagonal entry is the positive sum of all the permeances connecting that node to the adjacent nodes. Thus, the sum of all the entries in each row is 0. The exception to this occurs for nodes on the tangential boundaries of periodic models with odd symmetry. For models with odd symmetry, the off-diagonal entries corresponding to the permeances crossing the tangential boundaries become positive. Since each row only has 7 nonzero entries (except for the rows corresponding to the nodes on radial or axial boundaries, which have less than 7 nonzero entries), $\mathcal{P}_{3D}$ is a very sparse matrix.

III. The 3D Permeance Matrix

$\mathcal{P}_{3D}$, can be constructed in a general form with its constituent submatrices as shown in this section. The arrangement of these matrices is based on the MEC model node numbering system in which the first N_{2D} rows and the first N_{2D} columns in $\mathcal{P}_{3D}$ correspond to the nodes in the first axial layer, and the next N_{2D} rows and the next N_{2D} columns correspond to the nodes in the second axial layer, and so on. Within each set of N_{2D} rows or columns, the first N_{AL}, which is the number of angular or circumferential layers in the model, rows or columns correspond to nodes in the first radial layer of that axial layer, and the next N_{AL} rows or columns correspond to nodes in the second radial layer of that axial layer, and so on, as was the case for the organization of a single 2D MEC system permeance matrix, $\mathcal{P}_{2D}$ [14].

$\mathcal{P}_{3D}$ can be formed using the 2D permeance matrices developed in [14] and some additional diagonal matrices that represent the permeances of the axial flux tubes between 2D layers as submatrices, as shown in

$$\mathcal{P}_{3D} = \begin{bmatrix} \mathcal{P}_{2D(1)} + \mathcal{P}_{Ax(1:2)} & -\mathcal{P}_{Ax(1:2)} & 0 & \cdots & 0 \\ -\mathcal{P}_{Ax(1:2)} & \mathcal{P}_{Ax(1:2)} + \mathcal{P}_{2D(2)} + \mathcal{P}_{Ax(2:3)} & \ddots & \ddots & \vdots \\ 0 & \ddots & \ddots & \ddots & 0 \\ \vdots & \ddots & \ddots & \mathcal{P}_{Ax(N_{ZL}-2:N_{ZL}-1)} + \mathcal{P}_{2D(N_{ZL}-1)} + \mathcal{P}_{Ax(N_{ZL}-1:N_{ZL})} & -\mathcal{P}_{Ax(N_{ZL}-1:N_{ZL})} \\ 0 & \cdots & 0 & -\mathcal{P}_{Ax(N_{ZL}-1:N_{ZL})} & \mathcal{P}_{Ax(N_{ZL}-1:N_{ZL})} + \mathcal{P}_{2D(N_{ZL})} \end{bmatrix} \quad (10)$$

$\mathcal{P}_{2D(i)}$ is the 2D cross-section permeance matrix for the i^{th} axial layer, as developed in [14], and $\mathcal{P}_{Ax(j:j+1)}$ is the matrix representing the axial permeances between the j^{th} and $(j+1)^{th}$ axial layers. $\mathcal{P}_{Ax(j:j+1)}$ is a diagonal matrix with the k^{th} diagonal element representing the axial permeance between the k^{th} nodes in the j^{th} and $(j+1)^{th}$ axial layers.

The previous paragraph provides a general approach to forming $\mathcal{P}_{3D}$. However, due to the assumption of magnetic linearity and the geometry of the radial flux magnetic gear (assuming that all gear components have the same axial length), all of the axial layers inside the gear are identical to each other, except for potentially having different axial heights, and all of the axial layers outside the gear are also identical to each other, except for potentially having different axial heights. Therefore, the rest of this section presents an approach to forming $\mathcal{P}_{3D}$ that uses this fact to limit the number of permeance calculations required by scaling the permeances for each axial layer based on that layer's axial height.

The first three submatrices used in the construction of $\mathcal{P}_{3D}$ correspond to permeances inside the active gear geometry and are given by

$$\mathcal{P}_{Ax,IG} = \begin{bmatrix} \mathcal{P}_{Ax,IG(1:1)} & 0 & \cdots & 0 \\ 0 & \mathcal{P}_{Ax,IG(2:2)} & \ddots & \vdots \\ \vdots & \ddots & \ddots & 0 \\ 0 & \cdots & 0 & \mathcal{P}_{Ax,IG(N_{2D}:N_{2D})} \end{bmatrix} \quad (11)$$

$$\mathcal{P}_{IG(m:m-1)} = \mathcal{P}_{IG(m-1:m)} = \frac{2\mathcal{P}_{Ax,IG}}{h_{IG,m}+h_{IG,m-1}} \quad (12)$$

$$\mathcal{P}_{IG(m:m)} = h_{IG,m}\mathcal{P}_{2D,IG}. \quad (13)$$

$\mathcal{P}_{Ax,IG}$, defined in (11), is an (N_{2D} x N_{2D}) matrix in which each diagonal entry, $\mathcal{P}_{Ax,IG(i:i)}$, contains the "per-meter" value of the axial permeance connected to the i^{th} node in each 2D layer, assuming that the axial flux tubes are one meter long and contained entirely in the gear (and not the region outside of the gear). All off-diagonal entries in $\mathcal{P}_{Ax,IG}$ are zero. The (N_{2D} x

N_{2D}) axial permeance matrix, $\mathcal{P}_{IG(m:m\text{-}1)}$, corresponding to the axial permeances connecting in-gear axial layer m to in-gear axial layer m-1 can then be formed from $\mathcal{P}_{Ax,IG}$, according to (12). The scaling term used in (12) is the inverse of the appropriate axial path length, which is the average of the axial height of in-gear axial layer m, $h_{IG,m}$, and the axial height of in-gear axial layer m-1, $h_{IG,m\text{-}1}$. As indicated in (13), the (N_{2D} x N_{2D}) matrix of radial and tangential permeances corresponding to in-gear axial layer m, $\mathcal{P}_{IG(m:m)}$, is formed by scaling the 2D MEC in-gear system permeance matrix, $\mathcal{P}_{2D,IG}$, by the height of in-gear axial layer m. The matrix $\mathcal{P}_{2D,IG}$ is formed exactly as it is in a 2D MEC model, assuming a unit height [14].

There is an analogous out-of-gear permeance matrix corresponding to each of the three previously described in-gear permeance matrices. The matrix $\mathcal{P}_{Ax,OG}$ is defined similarly to $\mathcal{P}_{Ax,IG}$ in (11) as an (N_{2D} x N_{2D}) matrix in which each diagonal entry, $\mathcal{P}_{Ax,OG(i:i)}$, contains the "per-meter" value of the axial permeance connected to the i^{th} node in each 2D layer, assuming that the axial flux tubes are one meter long and contained entirely in the region outside of the gear. As was the case with $\mathcal{P}_{Ax,IG}$, all off-diagonal entries in $\mathcal{P}_{Ax,OG}$ are zero. The (N_{2D} x N_{2D}) axial permeance matrix, $\mathcal{P}_{OG(m:m\text{-}1)}$, corresponding to the axial permeances connecting out-of-gear axial layer m to out-of-gear axial layer m-1 can then be formed by scaling $\mathcal{P}_{Ax,OG}$, similarly to $\mathcal{P}_{IG(m:m\text{-}1)}$ in (12), where the scaling factor is the inverse of the appropriate axial path length, which is the average of the axial height of out-of-gear axial layer m, $h_{OG,m}$, and the axial height of out-of-gear axial layer m-1, $h_{OG,m\text{-}1}$. As in (13), the (N_{2D} x N_{2D}) matrix of radial and tangential permeances corresponding to out-of-gear axial layer m, $\mathcal{P}_{OG(m:m)}$, is formed by scaling the 2D MEC out-of-gear system permeance matrix, $\mathcal{P}_{2D,OG}$, by the height of out-of-gear axial layer m. $\mathcal{P}_{2D,OG}$ is formed in the same manner as $\mathcal{P}_{2D,IG}$, but all of the permeabilities used in the individual permeance calculations are set to μ_0 because the flux tubes are located entirely in nonmagnetic material.

All of the preceding terms correspond to permeances located either entirely in the active gear region or entirely in the region outside of the gear. However, the set of equivalent axial permeances connecting the last (top) in-gear axial layer to the first (bottom) out-of-gear axial layer, is formed by the series connection of the axial permeances corresponding to the top half of the last in-gear axial layer and the axial permeances corresponding to the bottom half of the first out-of-gear axial layer. $\mathcal{P}_{Bound}$ is an (N_{2D} x N_{2D}) diagonal matrix, representing these boundary axial permeances. Each diagonal entry, $\mathcal{P}_{Bound(i:i)}$, contains the equivalent axial permeance connecting the i^{th} node in the last in-gear axial layer to the i^{th} node in the first out-of-gear axial layer. As defined in

$$\mathcal{P}_{Bound(i:i)} = \left(\frac{h_{IG,N_{LIG}}}{2\mathcal{P}_{Ax,IG(i:i)}} + \frac{h_{OG,1}}{2\mathcal{P}_{Ax,OG(i:i)}} \right)^{-1}, \tag{14}$$

each diagonal entry, $\mathcal{P}_{Bound(i:i)}$, is formed by the scaled series combination of the corresponding diagonal entries in $\mathcal{P}_{Ax,IG}$ and $\mathcal{P}_{Ax,OG}$ ($\mathcal{P}_{Ax,IG(i:i)}$ and $\mathcal{P}_{Ax,OG(i:i)}$). All off-diagonal entries in $\mathcal{P}_{Bound}$ are zero.

The portion of $\mathcal{P}_{3D}$ corresponding to the in-gear nodes is constructed according to

$$\mathcal{P}_{3D,Ax,IG} = \begin{bmatrix} \mathcal{P}_{IG(1:2)} & -\mathcal{P}_{IG(1:2)} & 0 & \cdots & 0 \\ -\mathcal{P}_{IG(2:1)} & \mathcal{P}_{IG(2:1)} + \mathcal{P}_{IG(2:3)} & \ddots & \ddots & \vdots \\ 0 & \ddots & \ddots & \ddots & 0 \\ \vdots & \ddots & \ddots & \ddots & -\mathcal{P}_{IG(N_{LIG}-1:N_{LIG})} \\ 0 & \cdots & 0 & -\mathcal{P}_{IG(N_{LIG}-1:N_{LIG})} & \mathcal{P}_{IG(N_{LIG}-1:N_{LIG})} + \mathcal{P}_{Bound} \end{bmatrix} \tag{15}$$

$$\mathcal{P}_{3D,CS,IG} = \begin{bmatrix} \mathcal{P}_{IG(1:1)} & 0 & \cdots & 0 \\ 0 & \mathcal{P}_{IG(2:2)} & \ddots & \vdots \\ \vdots & \ddots & \ddots & 0 \\ 0 & \cdots & 0 & \mathcal{P}_{IG(N_{LIG}:N_{LIG})} \end{bmatrix} \tag{16}$$

$$\mathcal{P}_{3D,IG} = \mathcal{P}_{3D,Ax,IG} + \mathcal{P}_{3D,CS,IG}. \tag{17}$$

The ($N_{LIG}N_{2D}$ x $N_{LIG}N_{2D}$) matrix $\mathcal{P}_{3D,Ax,IG}$, defined in (15), contains the coefficients corresponding to axial permeances connected to in-gear nodes. Each diagonal submatrix entry $\mathcal{P}_{3D,Ax,IG(m,m)}$ in $\mathcal{P}_{3D,Ax,IG}$ contains the sum of the diagonal axial permeance matrices corresponding to axial permeances connected to nodes in the m^{th} in-gear axial layer. Each individual diagonal entry $\mathcal{P}_{3D,Ax,IG(i,i)}$ in $\mathcal{P}_{3D,Ax,IG}$ contains the sum of all equivalent axial permeances connected to the i^{th} in-gear node. These diagonal entries are analogous to the permeance coefficient of $\mathcal{F}_x$ in (7). Each off-diagonal submatrix entry, $\mathcal{P}_{3D,Ax,IG(m,n)}$, in $\mathcal{P}_{3D,Ax,IG}$ (entries where $m \neq n$) contains the negative diagonal axial permeance matrix corresponding to axial permeances connecting the m^{th} in-gear axial layer to the n^{th} in-gear axial layer. Each individual off-diagonal entry, $\mathcal{P}_{3D,Ax,IG(i,j)}$, in $\mathcal{P}_{3D,Ax,IG}$ (entries where $i \neq j$) contains the negative value of the equivalent axial permeance connecting the i^{th} in-gear node to the j^{th} in-gear node. These off-diagonal entries are analogous to the permeance coefficients of $\mathcal{F}_5$ and $\mathcal{F}_6$ in (7). Thus, for the in-gear nodes, $\mathcal{P}_{3D,Ax,IG}$ represents the terms on the left side of (7), excluding $\Phi_{x,2D}$. The ($N_{LIG}N_{2D}$ x $N_{LIG}N_{2D}$) matrix $\mathcal{P}_{3D,CS,IG}$, defined in (16), contains the coefficients corresponding to permeances connected to in-gear nodes within their own cross-sectional 2D layer (radial and tangential permeances, but not axial permeances). Each submatrix entry, $\mathcal{P}_{3D,CS,IG(m,m)}$, on the diagonal of $\mathcal{P}_{3D,CS,IG}$ is the 2D MEC system permeance matrix corresponding to the m^{th} 2D in-gear cross-sectional layer. These submatrices are analogous to the permeance coefficients in the $\Phi_{x,2D}$ term of (7), as defined in (8). The portion of $\mathcal{P}_{3D}$

corresponding to the in-gear nodes, $\mathcal{P}_{3D,IG}$, is formed by adding these submatrices as shown in (17). Note that the first submatrix row of $\mathcal{P}_{3D,Ax,IG}$ only uses a single diagonal axial submatrix, $\mathcal{P}_{IG(1:2)}$. This is due to the previously discussed use of a "half-stack" fractional model based on the gear's symmetry about the z-plane corresponding to its axial center. This effectively imposes the necessary zero axial flux boundary condition on the axial bottom of the "half-stack" model (the axial middle of the full stack gear model). If designs without this symmetry need to be evaluated, such as those with skewed magnets or axial misalignment, the 3D MEC system permeance matrix can easily be adjusted, using the same basic formation process, to model the full gear stack and two regions outside of the gear (one on each axial end).

Again, there is an analogous out-of-gear permeance matrix corresponding to each of the three previously described in-gear permeance matrices, and the portion of $\mathcal{P}_{3D}$ corresponding to the out-of-gear nodes is constructed similarly. The ($N_{LOG}N_{2D}$ x $N_{LOG}N_{2D}$) matrix $\mathcal{P}_{3D,Ax,OG}$ contains the coefficients corresponding to axial permeances connected to out-of-gear nodes. $\mathcal{P}_{3D,Ax,OG}$ can be defined similarly to $\mathcal{P}_{3D,Ax,IG}$ in (15); however, the $\mathcal{P}_{Bound}$ submatrix is added to the upper left term instead of the bottom right term. Each diagonal submatrix entry, $\mathcal{P}_{3D,Ax,OG(m,m)}$, in $\mathcal{P}_{3D,Ax,OG}$ contains the sum of the diagonal axial permeance matrices corresponding to axial permeances connected to nodes in the m^{th} out-of-gear axial layer. Each individual diagonal entry, $\mathcal{P}_{3D,Ax,OG(i,i)}$, in $\mathcal{P}_{3D,Ax,OG}$ contains the sum of all equivalent axial permeances connected to the i^{th} out-of-gear node. Each off-diagonal submatrix entry, $\mathcal{P}_{3D,Ax,OG(m,n)}$, in $\mathcal{P}_{3D,Ax,OG}$ (entries where $m \neq n$) contains the negative diagonal axial permeance matrix corresponding to axial permeances connecting the m^{th} and n^{th} out-of-gear axial layers. Each individual off-diagonal entry, $\mathcal{P}_{3D,Ax,OG(i,j)}$, in $\mathcal{P}_{3D,Ax,OG}$ (entries where $i \neq j$) contains the negative value of the equivalent axial permeance connecting the i^{th} and j^{th} out-of-gear nodes. The ($N_{LOG}N_{2D}$ x $N_{LOG}N_{2D}$) matrix $\mathcal{P}_{3D,CS,OG}$ can be defined similarly to $\mathcal{P}_{3D,CS,IG}$ in (16) and contains the coefficients corresponding to permeances connected to out-of-gear nodes within their own cross-sectional 2D layer (radial and tangential permeances, but not axial permeances). Each diagonal submatrix entry, $\mathcal{P}_{3D,CS,OG(m,m)}$, in $\mathcal{P}_{3D,CS,OG}$ is the 2D MEC system permeance matrix corresponding to the m^{th} 2D out-of-gear cross-sectional layer. The portion of $\mathcal{P}_{3D}$ corresponding to the out-of-gear nodes, $\mathcal{P}_{3D,OG}$, is formed by adding these submatrices similarly to the formation of $\mathcal{P}_{3D,IG}$ in (17).

The ($N_{LIG}N_{2D}$ x $N_{LOG}N_{2D}$) matrix $\mathcal{P}_{3D,Bound}$, defined in

$$\mathcal{P}_{3D,Bound} = \begin{bmatrix} 0 & \cdots & \cdots & 0 \\ \vdots & \ddots & \ddots & \vdots \\ 0 & \ddots & \ddots & \vdots \\ \mathcal{P}_{Bound} & 0 & \cdots & 0 \end{bmatrix}, \tag{18}$$

contains the portion of the overall 3D MEC system permeance matrix corresponding solely to the boundary axial permeances connecting nodes in the top in-gear layer and the bottom out-of-gear layer. All of the entries in this matrix are zeros, except for the single submatrix $\mathcal{P}_{Bound}$ in the corner. $\mathcal{P}_{3D}$ is created from the submatrices $\mathcal{P}_{3D,Bound}$, $\mathcal{P}_{3D,Bound}^{\mathrm{T}}$ (the transpose of $\mathcal{P}_{3D,Bound}$), $\mathcal{P}_{3D,IG}$, and $\mathcal{P}_{3D,OG}$, in the arrangement indicated by

$$\mathcal{P}_{3D} = \left[\begin{array}{c|c} \mathcal{P}_{3D,IG} & -\mathcal{P}_{3D,Bound} \\ \hline -\mathcal{P}_{3D,Bound}^{\mathrm{T}} & \mathcal{P}_{3D,OG} \end{array}\right]. \tag{19}$$

$\mathcal{P}_{3D}$ is always symmetric because all permeances in the MEC are bidirectional.

Each node in the 3D MEC has six adjacent nodes: one on the radial inside, one on the radial outside, one on the clockwise circumferential side, one on the counterclockwise circumferential side, one on the axial bottom side, and one on the axial top side. The only exceptions to this rule are the nodes in the innermost radial layer, which do not have any adjacent nodes on the radial inside, the nodes in the outermost radial layer, which do not have any adjacent nodes on the radial outside, the nodes in the bottom in-gear axial layer, which do not have any adjacent nodes on the axial bottom side, and the nodes in the top out-of-gear axial layer, which do not have any adjacent nodes on the axial top side. In light of this observation and close inspection of the matrices defined in (10)-(19), it is evident that each row in $\mathcal{P}_{3D}$ which does not correspond to one of these boundary layers has seven non-zero entries, one for each adjacent node, as well as the diagonal entry in each row. Thus, 3D MEC permeance matrices are even sparser than 2D MEC permeance matrices; therefore, the MATLAB implementation of the MEC model stores $\mathcal{P}_{3D}$ as a sparse matrix in order to dramatically reduce the requisite amount of memory used by the program.

IV. Solving the System

The 3D MEC model is "solved" by solving the linear system of equations given in (9) for the N_{3D} unknown node MMFs in the column vector $\mathcal{F}_{3D}$. As indicated in the description of the 2D MEC implementation [14], if the 3D MEC model has cross-sectional periodic symmetry, then it can be analyzed by solving the subset of equations corresponding to nodes in a symmetrical periodic fraction of the "half-stack" model and extending that solution to the remaining symmetrical fraction(s). Additionally, the same rules for the treatment of a reference node provided in the discussion of the 2D MEC solution [14] also apply to the 3D MEC solution.

Ideally, the MEC system can be solved by inverting the appropriate part of the system permeance matrix to solve for the node MMFs throughout a symmetrical periodic fraction of the magnetic gear. However, the 3D MEC system is much larger than its corresponding 2D MEC system; therefore, it is even less feasible to simply invert the 3D MEC system matrix due to the computational time and memory requirements. In order to mitigate these issues, the MATLAB implementation

of the 3D MEC model uses the same approach applied in the 2D MEC [14] and solves the system by factorizing the system permeance matrix and solving the corresponding triangular systems as described in [48]. The use of sparse matrices and an optimal factorization method are even more beneficial with respect to memory requirements and simulation run times for the solution of 3D MEC models.

Once a 3D MEC model has been "solved" for the vector of node MMFs, this information can be used along with the reluctances of the flux tubes to calculate various other quantities of interest, such as the flux in any flux tube and the flux density at any position in the gear. Like the 2D MEC model, the 3D MEC model also uses Maxwell stress tensors for torque calculations. In particular, the torque on the HSR, τ_{HSR}, and the torque on the LSR, τ_{LSR}, are calculated using Maxwell stress tensors according to

$$\tau_{HSR} = 2\left(\frac{r_{HS}^2}{\mu_0}\right)\int_0^{L/2}\int_0^{2\pi} B_r(r_{HS},\theta,z)B_\theta(r_{HS},\theta,z)d\theta dz \quad (20)$$

$$\tau_{LSR} = -2\left(\frac{r_{LS}^2}{\mu_0}\right)\int_0^{L/2}\int_0^{2\pi} B_r(r_{LS},\theta,z)B_\theta(r_{LS},\theta,z)d\theta dz, \quad (21)$$

where r_{HS} and r_{LS} represent the radii of the integration paths in the high speed air gap and low speed air gap, while B_r and B_θ represent the radial and tangential components of the magnetic flux density, which are both functions of the position in the gear. L denotes the axial length of the full stack model (including the regions beyond both axial ends of the gear). This implementation of the 3D MEC uses a symmetrical "half-stack" model; therefore, the torques are calculated by integrating the Maxwell stress tensor over the full axial length of the "half stack" model (from $z = 0$ to $z = L/2$) and doubling that torque to account for the other half of the stack. The torque on the entire modulator structure, τ_{Mods}, is then given by

$$\tau_{Mods} = -(\tau_{HSR} + \tau_{LSR}). \quad (22)$$

V. Conclusions

This is the first part of a two-part paper on the extension of an existing 2D linear MEC or reluctance network model [14] for radial flux magnetic gears to a 3D model. This part presents the systematic discretization of the magnetic gear geometry into node cells. In addition to the radial and angular layers for the 2D model, the 3D model divides the geometry into axial layers, both within and outside of the gear. The intersection of a radial layer, an angular layer, and an axial layer forms a node cell. For each node cell, Gauss's Law for magnetism is used to write an equation relating the potential of each node with the potentials of the adjacent nodes, based on the permeances of the flux tubes between the nodes and the equivalent fluxes injected by the presence of any permanent magnets. These equations are arranged into a very sparse matrix equation, which can be solved for the node potentials. Then, the fluxes and flux densities can be calculated to determine quantities of interest, such as torques.

Several factors can be employed to accelerate this process. First, assuming negligible axial misalignment, symmetry results in no axial flux crossing the axial middle of the gear. Thus, only the region outside the gear on one axial end and half of the gear's stack need to be included in the model. Second, because the cross-section of each axial layer in the gear is the same, and the cross-section of each axial layer in the region outside the gear is the same, the system matrix can be assembled from a few different submatrices and scaled based on the axial height of each axial layer. Third, as with the 2D model, periodic symmetry can be used to only evaluate a fraction of the geometry, reducing the number of angular layers required [14]. Finally, solving the matrix equation using efficient methods can result in significant reductions in the required time and computational memory [48].

The second part of this two-part paper compares the MEC model against FEA for different designs and different stack lengths. This is used to develop guidelines for choosing the axial layer distributions inside the gear and in the region axially beyond the gear. Additionally, the second part of this two-part paper evaluates the torque prediction accuracy of the 3D MEC model against 2D and 3D FEA for a parametric design study with 144,000 cases, which demonstrates the accuracy and usefulness of the 3D MEC model.

VI. References

[1] K. Atallah and D. Howe, "A Novel High-Performance Magnetic Gear," *IEEE Trans. Magn.,* vol. 37, no. 4, pp. 2844-2846, Jul. 2001.

[2] N. W. Frank and H. A. Toliyat, "Analysis of the Concentric Planetary Magnetic Gear with Strengthened Stator and Interior Permanent Magnet Inner Rotor," *IEEE Trans. Ind. Appl.,* vol. 47, no. 4, pp. 1652-1660, Jul.-Aug. 2011.

[3] P. O. Rasmussen, T. O. Andersen, F. T. Jorgensen, and O. Nielsen, "Development of a High-Performance Magnetic Gear," *IEEE Trans. Ind. Appl.,* vol. 41, no. 3, pp. 764-770, May-Jun. 2005.

[4] P. M. Tlali, R.-J. Wang, and S. Gerber, "Magnetic Gear Technologies: A Review," in *Proc. Int. Conf. Elect. Mach.*, 2014, pp. 544-550.

[5] J. J. Scheidler, V. M. Asnani and T. F. Tallerico, "NASA's Magnetic Gearing Research for Electrified Aircraft Propulsion," in *Proc. AIAA/IEEE Elect. Aircraft Technol. Symp*., 2018, pp. 1-12.

[6] N. W. Frank and H. A. Toliyat, "Gearing ratios of a magnetic gear for wind turbines," in Proc. *IEEE Int. Elect. Mach. Drives Conf*., 2009, pp. 1224–1230.

[7] K. K. Uppalapati, J. Z. Bird, D. Jia, J. Garner, and A. Zhou, "Performance of a magnetic gear using ferrite magnets for low speed ocean power generation," in *Proc. IEEE Energy Convers. Congr. Expo.*, 2012, pp. 3348–3355.

[8] N. W. Frank and H. A. Toliyat, "Gearing Ratios of a Magnetic Gear for Marine Applications," in *Proc. IEEE Electr. Ship Technol. Symp.*, 2009, pp. 477-481.

[9] T. V. Frandsen *et al*.,"Motor integrated permanent magnet gear in a battery electrical vehicle," *IEEE Trans. Ind. Appl*., vol. 51, no. 2, pp. 1516–1525, Mar./Apr. 2015.

[10] E. Gouda, S. Mezani, L. Baghli, and A. Rezzoug, "Comparative Study between Mechanical and Magnetic Planetary Gears," *IEEE Trans. Magn.,* vol. 47, no. 2, pp. 439-450, Feb. 2011.

[11] M. Johnson, M. C. Gardner, and H. A. Toliyat, "Design comparison of NdFeB and ferrite radial flux surface permanent magnet coaxial magnetic gears," *IEEE Trans. Ind. Appl.*, vol. 54, no. 2, pp. 1254–1263, Mar./Apr. 2018.

[12] M. C. Gardner, B. E. Jack, M. Johnson, and H. A. Toliyat, "Comparison of Surface Mounted Permanent Magnet Coaxial Radial Flux Magnetic Gears Independently Optimized for Volume, Cost, and Mass," *IEEE Trans. Ind. Appl.,* vol. 54, no. 3, pp. 2237-2245, May/June 2018.

[13] T. F. Tallerico, Z. A. Cameron, and J. J. Scheidler, "Design of a Magnetic Gear for NASA's Vertical Lift Quadrotor Concept Vehicle," in *Proc. AIAA/IEEE Elect. Aircraft Technol. Symp*., 2019, pp. 1-21.

[14] M. Johnson, M. C. Gardner, and H. A. Toliyat, "A Parameterized Linear Magnetic Equivalent Circuit for Analysis and Design of Radial Flux Magnetic Gears-Part I: Implementation," *IEEE Trans. Energy Convers.*, vol. 33, no. 2, pp. 784-791, June 2018.

[15] M. Johnson, M. C. Gardner, and H. A. Toliyat, "A Parameterized Linear Magnetic Equivalent Circuit for Analysis and Design of Radial Flux Magnetic Gears-Part II: Evaluation," *IEEE Trans. Energy Convers.*, vol. 33, no. 2, pp. 792-800, June 2018.
[16] M. Amrhein and P. T. Krein, "Magnetic Equivalent Circuit Modeling of Induction Machines Design-Oriented Approach with Extension to 3-D," in *Proc. IEEE Int. Elect. Mach. and Drives Conf.*, 2007, pp. 1557-1563.
[17] M. Amrhein and P. T. Krein, "3-D Magnetic Equivalent Circuit Framework for Modeling Electromechanical Devices," *IEEE Trans. Energy Convers.,* vol. 24, no. 2, pp. 397-405, Jun. 2009.
[18] M. Amrhein and P. T. Krein, "Force Calculation in 3-D Magnetic Equivalent Circuit Networks with a Maxwell Stress Tensor," *IEEE Trans. Energy Convers.,* vol. 24, no. 3, pp. 587-593, Sept. 2009.
[19] S. Gerber and R-J. Wang, "Analysis of the end-effects in magnetic gears and magnetically geared machines," in *Proc. IEEE Int. Conf. Elect. Mach.*, 2014, pp. 396-402.
[20] H. Y. Wong, J. Z. Bird, D. Barnett and W. Williams, "A High Torque Density Halbach Rotor Coaxial Magnetic Gear," in *Proc IEEE Int. Elect. Mach. Drives Conf.*, 2019, pp. 233-239.
[21] K. Li, S. Modaresahmadi, W. B. Williams, J. Z. Bird, J. D. Wright, and D. Barnett, "Electromagnetic Analysis and Experimental Testing of a Flux Focusing Wind Turbine Magnetic Gearbox," *IEEE Trans. Energy Convers*, vol. 34, no. 3, pp. 1512-1521, Sept. 2019.
[22] J. F. H. Douglas, "The Reluctance of Some Irregular Magnetic Fields," *Trans. AIEE,* vol. XXXIV, no. 1, pp. 1067-1134, Apr. 1915.
[23] E. R. Lwithwaite, "Magnetic Equivalent Circuits for Electrical Machines," *Proc. Inst. Electr. Eng.,* vol. 114, no. 11, pp. 1805-1809, Nov. 1967.
[24] C. J. Carpenter, "Magnetic Equivalent Circuits," *Proc. Inst. Electr. Eng.,* vol. 115, no. 10, pp. 1503-1511, Oct. 1968.
[25] V. Ostovic, "A Method for Evaluation of Transient and Steady State Performance in Saturated Squirrel Cage Induction Machines," *IEEE Trans. Energy Convers.,* vol. EC-1, no. 3, pp. 190-197, Sept. 1986.
[26] V. Ostovic, "Computation of Saturated Permanent-Magnet AC Motor Performance by Means of Magnetic Circuits," *IEEE Trans. Ind. Appl.,* vol. IA-23, no. 5, pp. 836-841, Sept. 1987.
[27] V. Ostovic, "A Novel Method for Evaluation of Transient States in Saturated Electric Machines," *IEEE Trans. Ind. Appl.,* vol. 25, no. 1, pp. 96-100, Jan.-Feb. 1989.
[28] C. B. Rasmussen and E. Ritchie, "A Magnetic Equivalent Circuit Approach for Predicting PM Motor Performance," in *Conf. Rec. IEEE Ind. Appl. Soc. Annu. Meeting*, 1997, pp. 10-17 vol.1.
[29] J. Perho, "Reluctance Network for Analysing Induction Machines," Ph.D. dissertation, Dept. Elect. and Commun. Eng., Helsinki Univ. Tech., Espoo, Finland, 2002.
[30] S. D. Sudhoff, B. T. Kuhn, K. A. Corzine, and B. T. Branecky, "Magnetic Equivalent Circuit Modeling of Induction Motors," *IEEE Trans. Energy Convers.,* vol. 22, no. 2, pp. 259-270, Jun. 2007.
[31] M. Yilmaz and P. T. Krein, "Capabilities of Finite Element Analysis and Magnetic Equivalent Circuits for Electrical Machine Analysis and Design," in *Proc. IEEE Power Electron. Specialists Conf.*, 2008, pp. 4027-4033.
[32] M. Amrhein and P. T. Krein, "Magnetic Equivalent Circuit Simulations of Electrical Machines for Design Purposes," in *Proc. IEEE Elect. Ship Technol. Symp.*, 2007, pp. 254-260.
[33] M. F. Hsieh and Y. C. Hsu, "A Generalized Magnetic Circuit Modeling Approach for Design of Surface Permanent-Magnet Machines," *IEEE Trans. Ind. Electron.,* vol. 59, no. 2, pp. 779-792, Feb. 2012.
[34] C. Bruzzese, D. Zito, and A. Tessarolo, "Finite Reluctance Approach: A Systematic Method for the Construction of Magnetic Network-Based Dynamic Models of Electrical Machines," in *Proc. AEIT Annu. Conf.*, 2014, pp. 1-6.
[35] L. Ding, G. Liu, Q. Chen, G. Xu, "A Novel Mesh-Based Equivalent Magnetic Network for Performance Analysis and Optimal Design of Permanent Magnet Machines," *IEEE Trans. Energy Convers.*, vol. 34, no. 3, pp. 1337-1346, Sep. 2019.
[36] D. Cao, W. Zhao, J. Ji, L. Ding, J. Zheng, "A Generalized Equivalent Magnetic Network Modeling Method for Vehicular Dual-Permanent-Magnet Vernier Machines," *IEEE Trans. Energy Convers.*, vol. 34, no. 4, pp. 1950-1962, Dec. 2019.
[37] S. Hlioui, B. Nedjar, L. Vido, Y. Amara and M. Gabsi, "2D–3D Magnetic equivalent circuit of the flux focusing permanent magnets synchronous machine," in *Proc. Int. Conf. Electr. Sci. and Tech. Maghreb*, 2014, pp. 1-7.
[38] V. Ostovic, *Dynamics of Saturated Electric Machines*, New York, NY, USA: Springer-Verlag, 1989.
[39] V. Ostovic, *The Art and Science of Rotating Field Machines Design*, Cham, Switzerland: Springer International Publishing, 2017.
[40] S. D. Sudhoff, *Power Magnetic Devices: A Multi-Objective Design Approach*, Hoboken, NJ, USA: John Wiley & Sons, 2014.
[41] M. Fukuoka, K. Nakamura, and O. Ichinokura, "Dynamic Analysis of Planetary-Type Magnetic Gear Based on Reluctance Network Analysis," *IEEE Trans. Magn.,* vol. 47, no. 10, pp. 2414-2417, Oct. 2011.
[42] M. Fukuoka, K. Nakamura, and O. Ichinokura, "A Method for Optimizing the Design of SPM Type Magnetic Gear Based on Reluctance Network Analysis," in *Proc. Int. Conf. Elect. Mach.*, 2012, pp. 30-35.
[43] D. Thyroff, S. Meier, and I. Hahn, "Modeling Integrated Magnetic Gears Using a Magnetic Equivalent Circuit," in *Proc. Annu. Conf. IEEE Ind. Electron. Soc.*, 2015, pp. 2904-2908.
[44] R. Benlamine, T. Hamiti, F. Vangraefschepe, F. Dubas, and D. Lhotellier, "Modeling of a Coaxial Magnetic Gear Equipped with Surface Mounted PMs Using Nonlinear Adaptive Magnetic Equivalent Circuits," in *Proc. Int. Conf. Elect. Mach.*, 2016, pp. 1888-1894.
[45] M. C. Gardner, D. A. Janak and H. A. Toliyat, "A parameterized linear magnetic equivalent circuit for air core radial flux coaxial magnetic gears with Halbach arrays," in *Proc. IEEE Energy Convers. Congr. and Expo.*, 2018, pp. 2351-2358.
[46] M. Desvaux, S. Sire, S. Hlioui, H. Ben Ahmed and B. Multon, "Development of a Hybrid Analytical Model for a Fast Computation of Magnetic Losses and Optimization of Coaxial Magnetic Gears," *IEEE Trans. Energy Convers.*, vol. 34, no. 1, pp. 25-35, March 2019.
[47] R. C. Holehouse, K. Atallah, and J. Wang, "A Linear Magnetic Gear," in *Proc. Int. Conf. Elect. Mach.*, 2012, pp. 563-569.
[48] T. A. Davis, "Algorithm 930: FACTORIZE: An Object-Oriented Linear System Solver for MATLAB," *ACM Trans. Math. Softw.,* vol. 39, no. 4, pp. 1-18, Jul. 2013.

VII. Biographies

Matthew Johnson (S' 13, M'17) earned his B.S. and Ph.D. both in electrical engineering from Texas A&M University, College Station, Texas, in 2011 and 2017, respectively. He is currently an electronics engineer for the U.S. Army Research Laboratory. His research interests include the design and control of electric machines and magnetic gears.

Matthew C. Gardner (S'15, M'19) earned his B.S. in electrical engineering from Baylor University, Waco, Texas in 2014. He earned his Ph.D. in electrical engineering from Texas A&M University, College Station, Texas in 2019. In August 2020, he joined the University of Texas at Dallas, where he is an assistant professor. His research interests include optimal design and control of electric machines and magnetic gears.

Hamid A. Toliyat (S'87, M'91, SM'96, F'08) received the B.S, degree from Sharif University of Technology, Tehran, Iran in 1982, the M.S. degree from West Virginia University, Morgantown, WV in 1986, and the Ph.D. degree from University of Wisconsin-Madison, Madison, WI in 1991, all in electrical engineering. Following receipt of the Ph.D. degree, he joined the faculty of Ferdowsi University of Mashhad, Mashhad, Iran as an Assistant Professor of Electrical Engineering. In March 1994 he joined the Department of Electrical and Computer Engineering, Texas A&M University where he is currently the Raytheon endowed professor of electrical engineering. Dr. Toliyat has many papers and awards to his name, including the Nikola Tesla Field Award.